

pubs.acs.org/crystal Article

Cooperative Rotational Motion Triggered by a Water Switch: Dehydration and Rehydration of Cytosine Monohydrate

Megan E. Fleming, Taylor A. Watts, Kelly A. McKenna, Elizabeth K. Miehls, and Jennifer A. Swift*



Cite This: Cryst. Growth Des. 2022, 22, 7443-7451



Read Online

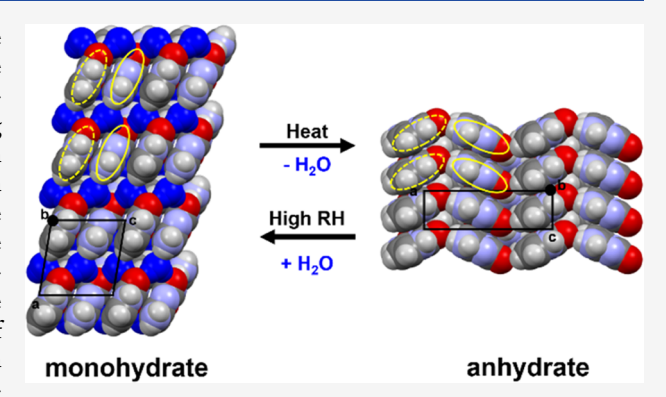
ACCESS I

Metrics & More

Article Recommendations

Supporting Information

ABSTRACT: Monohydrate and anhydrate crystalline forms of the DNA nucleobase cytosine interconvert via a topotactic solid-state mechanism where water functions as a molecular switch. The solidstate dehydration mechanism and kinetics were elucidated using complementary time-resolved synchrotron powder X-ray diffraction and thermogravimetric methods. Results indicate the reaction initiates from the crystal surface, involves no other crystalline intermediates, and proceeds at rates that depend on the monohydrate processing. A molecular-level model, based on leastmotion arguments and consistent with the totality of the experimental data, is proposed to account for the high degree of structure transfer associated with the transformation. Water loss on the monohydrate crystal surface activates the rotation of one-



dimensional cytosine ribbons, which in turn alters the local environment of the neighboring unit cell, facilitating the release of additional water molecules and ribbon rotation. As the dehydration front progresses into the solid, this cooperative mechanism effectively converts two-dimensional layers of antiparallel π -offset stacked ribbons into orthogonal two-dimensional layers of parallel π -face-face stacked ribbons. Moisture sorption experiments performed under high-humidity conditions confirm the anhydrate product can be reversibly rehydrated back to the monohydrate and that repeated dehydration-rehydration cycles proceed at consistent rates. The ability to track both the structural and compositional changes in the sample throughout the course of the reaction makes this a powerful combination of techniques for characterizing cooperative rotational motions triggered by water loss and/or uptake from crystalline materials.

INTRODUCTION

Chemists have a clear intellectual framework for thinking about reactions that occur in solution. The mechanism (e.g., substitution, elimination, addition, etc.) can be determined by varying parameters such as concentration, temperature, and/or solvent, with key intermediates sometimes identified through spectroscopy. In contrast, reactions that occur in the solid state involve large assemblies of molecules, each of which has several close neighbors whose local environments are affected by reaction at nearby sites. Mechanistic investigations of solid-state reactions are further complicated by the fact that they may be sensitive to additional factors such as particle size, shape, and crystalline defects.

Water uptake and loss are important processes that affect the physical properties of crystalline materials ranging from pharmaceuticals to food products to energetic materials. Solidstate dehydration reactions are typically investigated by monitoring the compositional changes related to weight/water loss over time and fitting that data to various kinetic solid-state reaction models. The models are mathematical representations of the rate-limiting step in the reaction, which could be the rate at which a reactive species diffuses into/out of the lattice (diffusion models), the rate of change at the reaction interface (phase boundary models), or the rate of product phase formation (nucleation and growth models).^{1,2} However, these general models do not take into account the local molecularlevel motions the organic components must undergo within the lattice. Establishing correlations between the initial and final structures has been possible in some cases, 3-6 but not frequently in parallel with kinetics-based approaches. Here, we couple these two solid-state mechanistic approaches—using both kinetic modeling and molecular-level structure correlation—to elucidate the cytosine hydrate—anhydrate solid-state transformation.

Owing to its importance as one of the four DNA nucleobases, studies on cytosine crystals date back to the 1960s, when monohydrate (CM, refcode: CYTOSM) and anhydrate (refcode: CYTSIN) structures were first reported.^{7,8} In the 1980s, Perrier and Byrn⁹ used hot-stage microscopy observa-

Received: September 8, 2022 Revised: October 27, 2022 Published: November 8, 2022





tions on single crystals of CM and other purine and pyrimidine hydrates in an effort to correlate the dehydration anisotropy with structural factors such as hydrogen bonding and water channel dimensions. Martel and Powell confirmed with powder X-ray diffraction (PXRD) that CM dehydration under near-physiologic temperatures yields the thermodynamically stable anhydrate as a final product. Kawasaki et al. 11,12 examined CM dehydration through the lens of spontaneous chirality generation. Recognizing that CM is centrosymmetric $(P2_1/c)$ but the anhydrate is chiral $(P2_12_12_1)$, they elegantly demonstrated that water removal through enantiotropic faces led to anhydrous products with opposite handedness. More recently, Braun et al. 13,14 used thermal analysis, IR spectroscopy, moisture sorption, PXRD, and crystal structure prediction methods to assess the thermal and moisture stability range of CM and its anhydrate.

Here, we seek to expand our molecular-level understanding of the transformation between cytosine monohydrate and anhydrate using a complementary battery of time-resolved methods including synchrotron powder X-ray diffraction (sPXRD), thermogravimetric analysis (TGA), and dynamic vapor sorption (DVS). Our results indicate that the hydrate-to-anhydrate reaction and its reverse occur via a cooperative "switch-like" mechanism, which progressively transforms one extended two-dimensional π -network into an orthogonal π -network with different symmetry. The effects of particle size on the reaction kinetics and mechanism are also considered.

$$\begin{array}{c|c} O \\ \hline \\ HN \\ 5 \\ 1 \\ \hline \\ 4 \\ 2 \\ \hline \\ NH_2 \\ \hline \\ Cytosine \\ \end{array}$$

■ EXPERIMENTAL METHODS

CM Sample Preparation. Anhydrous cytosine was obtained from Aldrich (\geq 99%) and used as received. Ultrapure deionized water (18 $\rm M\Omega)$ was used as the solvent in all relevant growth solutions. Cytosine monohydrate (CM) crystals were prepared by slow evaporation of saturated aqueous cytosine solutions (4 mg/mL). The supersaturated solutions were added to Pyrex Petri Culture Dishes (100 \times 10 mm²) and maintained at 25 \pm 1 °C. CM crystals typically appeared as rectangular plates with large (100) faces and smaller (010) and (001) side faces after \sim 24 h.

CM was used either as-grown and unground (UG), manually wetground using a mortar and pestle and a small amount of growth solution (WG) or ball-milled. A Retsch MM300 ball mill with Teflon chambers and zirconium milling media (Yttrium stabilized, 10 mm) was used to mill samples at 12 Hz for 1, 5, or 10 min.

Microscopy. Optical and hot-stage microscopy was performed using an Olympus BX-50 polarizing microscope fitted with a Lumenera Xfinity 2.0 camera attachment and Xfinity Analyze software (Lumenera, Ontario). Hot-stage microscopy was accomplished with an HCS302 optical hot-stage (INSTEC, Inc., Boulder, CO). Scanning electron microscopy (SEM) images were obtained on a Zeiss SUPRAS5-VP microscope. Samples were mounted on a 3.1 mm carbon-tape layered aluminum mount (Amray Instruments). All images were taken with an in-lens detector with an acceleration voltage of 1 kV.

Thermal Analysis (DSC and TGA). Differential scanning calorimetry data were obtained on a TA Instruments DSC Q25 equipped with a cooling system. DSC experiments were performed on 3.0–5.0 mg samples in hermetically sealed aluminum pans (TA Instruments). Samples (UG, WG, or milled) were measured in triplicate at 5.0 °C/min over the temperature range of 25–150 °C.

Thermogravimetric (TGA) data were obtained on a TA Instruments SDT Q600 or Q50 (New Castle, DE) using a nitrogen flow rate of 50 mL/min. All experiments used ~3.0 mg of CM (UG, WG, or milled) in open 90 μ L aluminum pans (TA Instruments). Isothermal experiments on unground CM were performed at 55, 60, and 65 °C, and on wetground CM at 50 and 55 °C. The fraction dehydrated, α , at any given time was determined from the wt % loss at each datapoint relative to the total wt % loss for each experiment (theoretical wt % = 13.9%).

Dynamic Vapor Sorption (DVS). Moisture sorption experiments were performed on a TA Instruments Q5000 Dynamic Vapor Sorption instrument using 5 mg samples in metalized quartz pans. In fixed relative humidity experiments at 25 °C, anhydrate weight changes were monitored at 75, 85, and 95% RH. Hydration—dehydration experiments were performed by cycling the %RH of the sample environment between 95% (120 min) and 5% RH (600 min) for a total of four cycles.

X-ray Diffraction. Powder X-ray diffraction (PXRD) data were collected using a DUO Apex X-ray diffractometer at room temperature. Powdered samples were prepared in Kapton capillaries (Cole-Parmer) with PXRD data collected using Cu K α radiation over a range $2\theta = 5-40^{\circ}$. CM single-crystal X-ray diffraction data were collected on a Bruker D8 Quest diffractometer using Mo K α radiation ($\lambda = 0.71073$ Å) at 100, 150, 200, 250, and 295 K. Structures were solved by intrinsic methods and refined using full-matrix least-squares on F^2 using SHELXT-Version 2014/5 and SHELXL-2018/3 software. CCDC deposition numbers: 2205653-2205657

Time-Resolved Synchrotron Powder X-ray Diffraction (sPXRD). All synchrotron powder X-ray diffraction data were collected on beamline 17-BM-B at the Advanced Photon Source. Experiments had an X-ray beam energy of 27 keV ($\lambda = 0.39433$ Å) and a beam size of 300 μ m. The beamline uses a Si (311) monochromator, a PerkinElmer a-Si Flat Panel PE1621 area detector, and an Oxford Cryosystems Cryostream 700+. Samples were ground in the mother liquor, loaded wet into a Kapton capillary ferrules, and stoppered with glass wool. Capillaries were then placed in a flow cell designed for in situ experiments. 16 In dehydration experiments, dry He (5 mL/min) was flowed continuously over the sample to remove the mother liquor and maintain an RH = 0% environment. Samples were rocked at 15° throughout the data collection. Exposure time was 2.0 s/image summed over 10 images, enabling collection of a high-Q-range PXRD pattern every 20 s. Experiments were performed under both isothermal (323-338 K) and variable-temperature (heating rate 3-10 K/min) conditions.

GSAS-II software 17 was used for data processing and 2D image integration. Powder refinements were completed using Pawley and Rietveld methods using TOPAS-V6 software. 18 Quantitative Rietveld refinements used the fundamental parameters approach. Refined global parameters included background and zero error terms; refined phase-specific parameters included a Rietveld scale factor, unit cell, crystallite size, and microstrain. The reaction conversion was determined directly from the refined ratio of phases. The phase ratio in TOPAS-V6 was determined using eq 1, where $x_{\rm p}$ is the weight fraction of phase p, $S_{\rm p}$ is the scale factor of phase p, $M_{\rm p}$ is the mass of unit cell of phase p, and $V_{\rm p}$ is the volume of unit cell of phase p. $^{19-21}$

$$x_{p} = \frac{S_{p}M_{p}V_{p}}{\sum_{i=1}^{m} (S_{i}M_{i}V_{i})}$$
(1)

Solid-State Kinetic Analyses. The kinetics of each solid-state dehydration (or rehydration) reaction was determined from the conversion as a function of time as measured by sPXRD, TGA, or DVS under isothermal conditions. For each method, the regions where the fraction dehydrated (α) was linear were used in kinetic analyses, typically 0.1 < α < 0.7 unless otherwise stated. All solid-state kinetic reaction models have the general form

$$\frac{\mathrm{d}\alpha}{\mathrm{d}t} = A\mathrm{e}^{-(E_a/RT)}f(\alpha) = k(T)f(\alpha) \tag{2}$$

where α is the fraction dehydrated (or rehydrated), A is the preexponential or frequency factor, E_a is the activation energy (J/

mol), $R = 8.314 \text{ JK}^{-1}\text{mol}^{-1}$, k(T) is the rate constant, and $f(\alpha)$ is the reaction model in its differential form. The integral form of eq 2 is

$$g(\alpha) = Ae^{-(E_a/RT)}t \tag{3}$$

The time-dependent data were then fit to each of the solid-state reaction models listed in Table 1 and statistically evaluated on the basis of the correlation coefficient (R^2) and the standard deviation in the slope of the regression line ($S_{\rm m}$). The $E_{\rm a}$ for each reaction was determined from the slope of Arrhenius plots created from the rate constants determined from top reaction models at each of three different isothermal temperatures (55–65 °C). Further analysis of the data with model-free Freidman methods ²² at several fixed points along the course of a reaction was used to verify a constant $E_{\rm a}$ throughout the reaction.

Table 1. Solid-State Reaction Models and Integral Expressions Used for Kinetic Analyses^{1,2}

reaction model	integral equation $g(\alpha) = kt$
Nucleation & Growth	
1D growth of nuclei (Avrami–Erofeev Eq, $n = 2$) (A2)	$(-\ln(1-\alpha))^{0.5}$
2D growth of nuclei (Avrami–Erofeev Eq. $n = 3$) (A3)	$(-\ln(1-\alpha))^{1/3}$
3D growth of nuclei (Avrami–Erofeev Eq. $n = 4$) (A4)	$(-\ln(1-\alpha))^{1/4}$
random nucleation (Prout-Tompkins Eq) (P1)	$\ln(\alpha/(1-\alpha)) + e^{\alpha}$
power law $(n = 1/2)$ (P2)	$lpha^{1/2}$
power law $(n = 1/3)$ (P3)	$lpha^{1/3}$
power law $(n = 1/4)$ (P4)	$lpha^{1/4}$
Geometrical Contraction	
zero-order (R1)	α
2D phase boundary (contracting area) (R2)	$1-(1-\alpha)^{1/2}$
3D phase boundary (contracting volume) (R3)	$1-(1-\alpha)^{1/3}$
Diffusion	
1D diffusion (D1)	α^2
2D diffusion (D2)	$(1-\alpha)*(\ln(1-\alpha)) + \alpha$
3D diffusion (Jander Eq) (D3)	$(1-(1-\alpha)^{1/3})^2$
3D Diffusion (Ginstling-Brounshtein Eq) (D4)	$(1-(2/3)*\alpha) - (1-\alpha)^{2/3}$
Reaction Order	
first-order (F1)	$-\ln(1-\alpha)$
second-order (F2)	$(1/(1-\alpha))-1$
third-order (F3)	$(1/2)*(((1-\alpha)^{-2})-1)$

■ RESULTS AND DISCUSSION

Cytosine monohydrate (CM) and anhydrous cytosine structures are shown in Figure 1, with different views to depict the major topological features of interest. Water molecules in CM are colored blue for clarity. In CM, cytosine molecules assemble into polar one-dimensional hydrogen-bonded ribbons formed via N···H-N and NH₂···O bonds (2.09 and 2.15 Å, respectively) which align parallel to the *b*-axis. Adjacent ribbons have an *antiparallel* orientation and through offset π stacking create dense centrosymmetric layers in the (100) plane. The view in Figure 1A is down the *c*-axis to visualize where the water sits relative to the dense (100) layers. The view in Figure 1B is down the *b*-axis which is end-on with respect to the ribbon direction. Solid and dashed green ovals identify the ribbons and their two orientations, which are related by 180°. The dense (100) layers are related by translation along the *a*-axis.

Water molecules in CM are too far apart to hydrogen-bond to one another ($O_w \cdots O_w$ 3.93Å), though they do hydrogen-bond to cytosine molecules through NH₂···O_w (2.13 Å) and O_w-H..O (2.04 and 1.95 Å) and therefore serve to connect adjacent layers and ribbons. Different authors have previously referred to CM as both a "channel hydrate" and an "isolated hydrate." This ambiguity arises in part because the minimum cross section to be considered a "channel" is not well defined. In the room temperature structure, there is unoccupied volume between water sites along the c-axis, though the cross-sectional diameter at the narrowest point between water sites is less than the molecule's kinetic diameter.²³

Anhydrous cytosine is shown in Figure 1C,D with views down the c-axis and b-axis, respectively. Cytosine molecules in the anhydrous form have the same one-dimensional hydrogenbonded ribbon motif as CM. The N···H-N bond length in the two forms are nearly identical (2.12 vs 2.09 Å) though the NH₂···O bond is slightly shorter in the anhydrate than in CM (1.90 Å vs 2.15 Å). Adjacent ribbons π stack face—face to create dense layers in the (100) plane. Since the ribbons in the anhydrate are related by translation and have a *parallel* orientation, the dense (100) planes are polar. Adjacent (100) layers are related by a twofold rotation. Therefore, while CM and the anhydrate share a common ribbon structure, the symmetry within their π -stacked layers is distinctly different.

CM Dehydration—Macroscopic Changes. CM single crystals grown from saturated aqueous solutions typically deposit in 2-3 days as clear, transparent rectangular plates with large (100) faces and smaller (001) and (010) side faces. Both optical microscopy and SEM show the CM crystal surfaces are relatively smooth (Figure 2A). When single CM crystals are heated under hot-stage microscopy conditions, dehydration is observed to initiate from several different spots on the outer edges of the crystal. The opaque reaction fronts expand moving inward over time until the entire crystal eventually darkens (Figure S1). Though the material retains the same macroscopic plate morphology after dehydration, it is clearly polycrystalline. SEM images of the dehydrated material revealed that the plate and side faces now exhibit distinctly different textures (2B). The plate face is the smoother of the two, though this surface has numerous deep cracks (2C). The cracks are irregular and form in multiple directions, though qualitatively the largest cracks have a slight bias to form along what was formerly the b-axis of CM. The side faces become extremely rough with a granular texture but do not generally exhibit large cracks.

Particle Size Effects. Individual CM crystals both within and across different growth batches typically exhibit some variability in their sizes, though at the outset of this study it was not clear to what extent particle size would affect the dehydration kinetics or mechanism(s). To assess the effect of particle size CM was processed using three different methods: as-grown and unground (UG), wet-ground in a mortar and pestle (WG), and ball-milled at 12 Hz for 1, 5, or 10 min.

SEM micrographs of samples WG, and milled for 1 and 5 min were similar, consisting of irregularly shaped particles with a distribution of sizes (Figure S2). The average particle size qualitatively decreased and the distribution became somewhat more uniform with longer 10-min milling times. However, PXRD of the 10-min-milled CM indicated the presence of some anhydrate. PXRD showed no evidence of form conversion in the WG, 1- or 5-min-milled samples.

Samples processed with each method were characterized with DSC. When unground CM was heated at 5 °C/min in

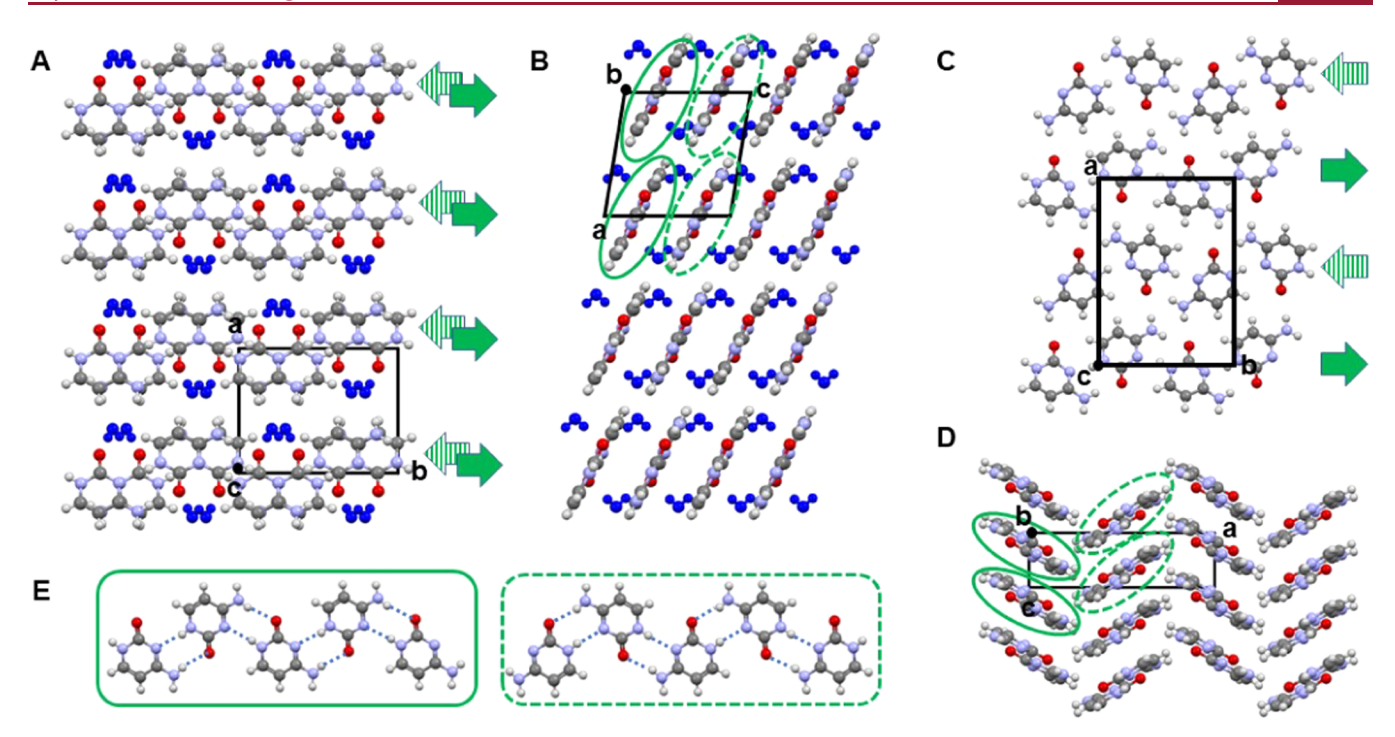


Figure 1. (A, B) Packing diagram of cytosine monohydrate (CM, refcode: CYTOSM11) viewed down the c-axis and b-axis, respectively. Water molecules are blue. The view along the c-axis helps to illustrate the orientation of the water molecules with respect to the dense π -stacked layers. The one-dimensional hydrogen-bonded cytosine ribbons are end-on when viewed down the b-axis. (C, D) Packing diagram of anhydrous cytosine (refcodes: CYTSIN01) viewed down the c-axis and b-axis, respectively. The latter is an end-on view of the one-dimensional cytosine ribbons. (E) Both structures share a common polar ribbon motif consisting of N···H-N and N-H····O bonds. The two possible ribbon orientations, which differ by 180°, are indicated by solid and dashed green ovals and arrows. Notably, dense (100) planes in CM are centrosymmetric, whereas the dense (100) planes in the anhydrate are polar.

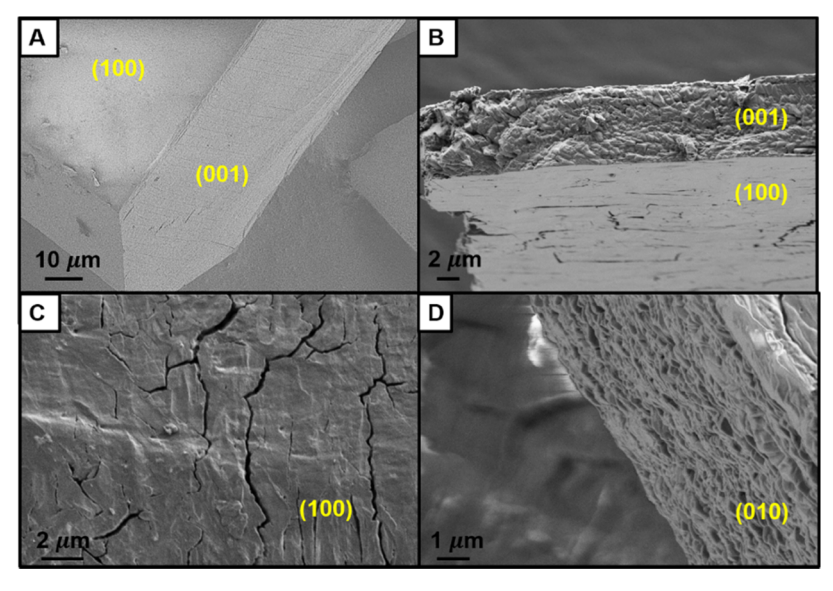


Figure 2. SEM images of CM before and after dehydration. (A) Before heating, all faces of CM single crystals are relatively smooth. (B–D) After CM is dehydrated, a notable change in the surface topology is observed, indicating polycrystallinity. Large irregular cracks develop on what was originally the plate face, and the side faces become very rough and take on a granular texture. All Miller indices refer to the original CM lattice.

hermetically sealed pans, a dehydration endotherm was observed with a $T_{\rm max}$ of 96.8 °C \pm 1.7 °C (C.I. = 95%) (Figure S3). $T_{\rm max}$'s measured for the WG and the milled samples were equivalent, though the standard deviation of all ground samples was slightly larger than that of unground material. Heating under TGA conditions in open pans indicated qualitatively faster weight loss in the ground material.

tion. To elucidate the structural changes that occur during the thermal dehydration of CM, we turned to time-resolved *in situ* synchrotron powder diffraction (sPXRD). CM samples were manually ground in a small amount of growth solution, loaded into Kapton capillaries, and maintained under a constant He gas flow of 5 mL/min (RH = 0%). With a data collection method

that enables a high-resolution pattern to be collected every ~ 20

Time-Resolved Structural Changes During Dehydra-

s, dehydration experiments were performed on CM by heating at a constant rate (3 or $10^\circ/\text{min}$) from room temperature to 445 K (172 °C) or by heating isothermally at 328, 333, and 338 K (55, 60, and 65 °C).

In all temperature ramped and isothermal experiments, CM dehydrated directly to one crystalline product, which we refer to as Cd. Reitveld refinement confirmed that product Cd has the same structure as the anhydrate previously described (Figure S4). There was no evidence of any other crystalline intermediate in the transformation process. A representative contour plot of 30 sPXRD patterns collected during a 10 °C/min temperature ramping experiment is shown in Figure 3. In this experiment, Cd is first detected at 88 °C and the CM-to-Cd conversion is complete within ~2 min. Dehydration under isothermal conditions at 55–65 °C required longer times (4–13 min) to reach completion. Isothermal dehydration was attempted at 50 °C, but no change in the sPXRD pattern was observed after an hour at this temperature.

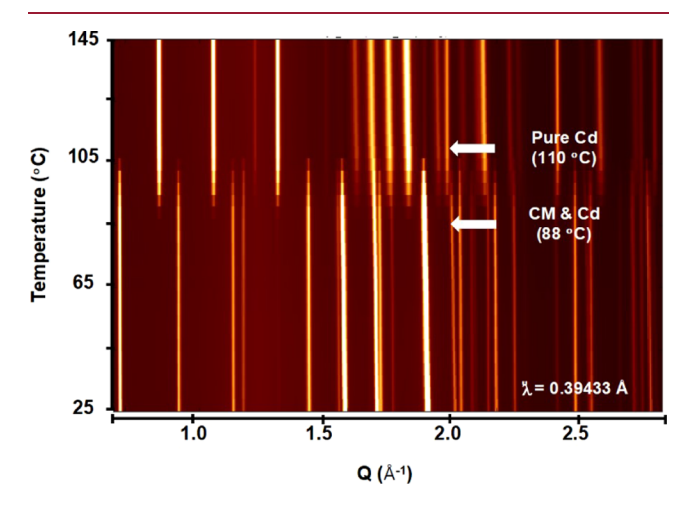


Figure 3. Contour plot constructed from 30 sPXRD patterns collected during CM dehydration when heated from 22 to 145 °C at 10 °C/min. The phase transformation is complete within ~ 2 min.

In a previous dehydration study on thymine hydrate,²⁷ sequential Rietveld refinement of sPXRD patterns collected under isothermal conditions revealed subtle changes in the hydrate lattice that indicated partial water loss preceded the appearance of anhydrate product. Using the same sequential Rietveld refinement methods here, we initially expected to see a similar effect in this system. However, no appreciable changes in the CM lattice parameters were observed in any of the isothermal dehydration datasets, either before the first appearance of Cd or during the transformation process. Refined unit cell parameters obtained from a 60 °C isothermal experiment are shown in Figure 4. Point "B" (orange datapoint) corresponds to the sPXRD pattern where Cd is present in \sim 1%. The consistency of the lattice parameters indicates that water loss from CM occurs simultaneously with, but not prior to, the formation of Cd.

Dehydration Mechanism and Kinetics. Having demonstrated that the dehydration involves no other crystalline intermediates, we sought to gain further mechanistic insight and extract kinetic parameters for the reaction. The reaction conversion over time was determined from sPXRD and TGA data obtained at the same isothermal temperatures (55, 60, and 65 °C). CM used in all isothermal sPXRD experiments was from

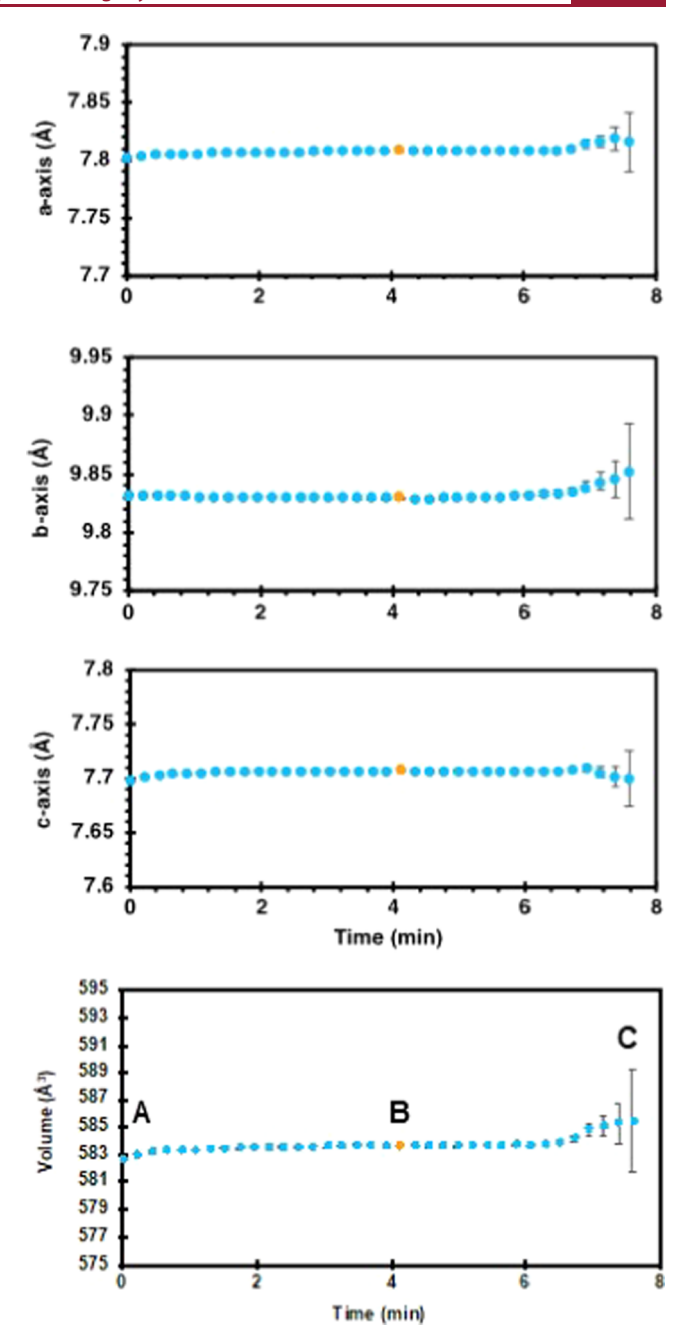


Figure 4. Unit cell parameters obtained from sequential refinement of sPXRD patterns collected at 60 $^{\circ}$ C during the solid-state transformation of CM to Cd. (A) CM = 100 wt %, (B) CM \sim 99 wt %, (C) CM \sim 0.5 wt %.

the same batch to minimize any particle size effects. The reaction progress was determined based on the CM/Cd phase ratio in sequentially refined sPXRD patterns. The reaction progress from TGA data was based on the time-dependent weight loss relative to the monohydrate water content (calc. 13.9%). At each temperature, replicate TGA datasets were collected. Plots of the fraction dehydrated (α) vs time appear in Figure 5 based on (top) sPXRD data refinement and (bottom) representative TGA measurements.

Both types of data show the same trends, though the sPXRD and TGA experimental conditions and the CM processing methods were not identical. The former was performed under He gas flow and used manually ground CM, while the latter was

 Crystal Growth & Design
 pubs.acs.org/crystal
 Article

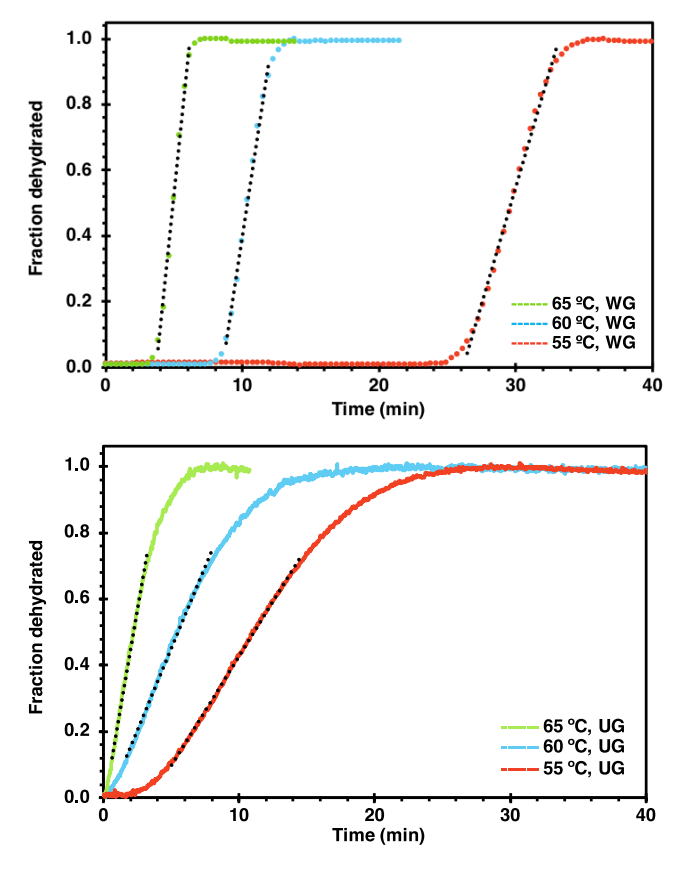


Figure 5. CM fraction dehydrated as a function of time when heated isothermally at 55, 60, and 65 °C. Data from (top) sequential refinement of sPXRD data and (bottom) TGA weight loss measurements.

done in open pans under N_2 gas and used unground CM. This was intentional since it provided an additional opportunity to assess how particle size may affect the reaction kinetics and/or mechanistic model fitting. TGA data were also collected on manually ground CM for comparison purposes.

The reaction conversion data at each isothermal temperature were used in model-based and model-free kinetic analyses. $^{1,2,28-30}$ Established model-based methods can provide insight into the most probable rate-limiting step in the reaction, whereas model-free methods allow for the determination of activation energy $(E_{\rm a})$ parameters at fixed time points throughout the reaction without any model assumptions. For the most complete description of the reaction, both methods were used together in this work.

The dehydration data in Figure 5 were fit to each of the reaction models listed in Table 1 and assessed based on correlation coefficients (R^2) and the standard deviation in the slope of the regression line ($S_{\rm m}$). While in other hydrate systems²⁷ it was possible to identify one "best fit" model, this was not the case for CM. sPXRD and TGA data fit equally well to several nucleation & growth (A2, A3, A4, and P1) and geometrical contraction (R1, R2, and R3) models (Table S1). sPXRD data had slightly higher correlation coefficients for nucleation & growth models A3, A4, and P1 ($R^2 > 0.999$) with geometrical contraction models R1, R2, and R3 ($R^2 > 0.999$) not far behind. Fits to the TGA data collected using unground CM, had the highest correlation coefficients for geometrical contraction models R1 and R2 ($R^2 > 0.999$) with nucleation & growth models A2, A3, A4, and P1 ($R^2 > 0.999$) not far behind.

Notably, diffusion models were a poor fit for all isothermal sPXRD and TGA data.

To assess how crystallite size impacts dehydration, TGA on manually ground CM was performed at 50 and 55 °C. The slightly lower temperatures were needed, as TGA experiments at \geq 60 °C on ground CM indicated dehydration began before the instrument could reach the isothermal temperature. When the 50 and 55 °C TGA data were fit to different reaction models, those with the highest R^2 were the same as those for unground CM. From this, we concluded that while the reaction rate is altered by grinding, the dehydration mechanism is not.

To get a better estimate of how particle size affects the reaction rate, we compared the rate constant at 55 °C determined from sPXRD (WG), TGA (WG), and TGA (UG) data (Table S2). Using model R1, a good fit for all isothermal experiments, the rate constants associated with dehydration of ground CM in the sPXRD (0.149 min⁻¹) and TGA (0.165 min⁻¹) datasets were very close. Not surprisingly, TGA on ground and unground CM yielded very different rate constants, with unground CM (0.067 min⁻¹) less than half that of the ground material.

With three isothermal data at three temperatures, the activation energy (E_2) of the solid-state reaction for unground and ground CM could also be calculated from the slope of an Arrhenius plot of $-\ln(k)$ vs 1/T. Fitting the sPXRD data to the four models with the highest correlation coefficients yielded E_a values between 92 \pm 7 and 99 \pm 6 kJ/mol. Model-free Friedman analysis of sPXRD data at fixed time points showed Ea is consistent over the entire reaction coordinate, with an average E_a of 96.4 ± 1.7 kJ/mol (Figure S5). TGA data collected on unground CM fit to the same four models yielded an E_a of 108– $109 \pm 12 \text{ kJ/mol}$ and a model-free E_a of $106 \pm 18 \text{ kJ/mol}$. That the UG material has a notably higher Ea points to a surfacemediated dehydration mechanism that is sensitive to particle size and/or shape effects. All grinding methods increase the surface area, though these processing steps can also create defects and is difficult to separate these two effects.

Water Switch. With knowledge that the CM-to-Cd transformation is a surface-mediated process that involves no intermediate phases, we return to the cytosine monohydrate and anhydrate structures to rationalize the molecular-level transformation pathway. Our proposed model assumes that the 1-D hydrogen-bonded ribbon motif (b-axis), which is common to both structures, is robust. This assumption is supported by thermal expansion data. The single-crystal structure of CM was determined at five temperatures between 100 and 295 K (Table S3). Over this temperature range, the expansion along the b-axis (0.27%) is minimal and much lower than either the a-axis (0.8%) or c-axis (2.6%) (Figure 6). This suggests that molecular mobility between ribbons along the a- and c-axes is greater than along the 1-D ribbon direction.

Each water molecule in the interior of a CM crystal connects three ribbons (Figure 7, blue lines). It serves as a hydrogen-bond donor to two adjacent ribbons in the same (100) plane (e.g., pink and gray ribbons) and as a hydrogen-bond acceptor to a tertiary amine in a ribbon in the adjacent (100) plane (e.g., yellow ribbon). When water leaves the lattice, water···cytosine hydrogen bonds are necessarily broken. For any three 1-D ribbons which were connected via hydrogen-bonded water, the donors and acceptors of two can be satisfied by the formation of C=O···H₂N hydrogen bonds between antiparallel ribbons (red dashed lines, e.g., between yellow and pink ribbons). To optimize the new inter-ribbon hydrogen bonding geometry, the

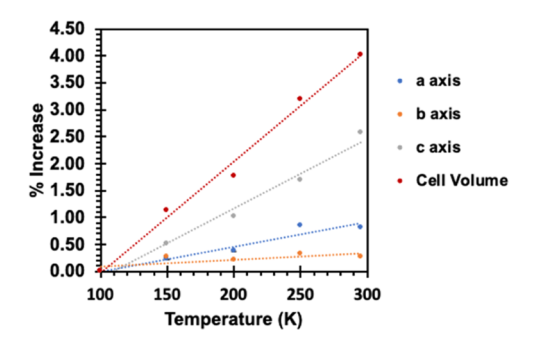


Figure 6. Thermal expansion of CM over the temperature range 100–295 K based on single-crystal structures determined at 100, 150, 200, 250, and 295 K.

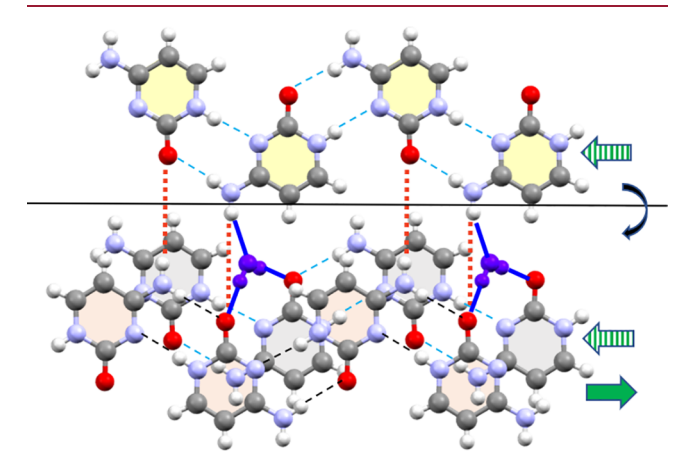


Figure 7. Schematic of the molecular-level reorganization in the CM-to-Cd reaction. Each water molecule (blue) is a hydrogen-bond donor to two 1-D ribbons in the (100) plane (pink and gray) and a hydrogen-bond acceptor to one 1-D ribbon above (yellow). Ribbon directions are indicated with green solid and striped arrows. When the water-cytosine bonds are broken, new hydrogen bonds (red) form between antiparallel ribbons. Rotation of the 1-D ribbons optimizes the binding geometry and creates new face—face π -stacks of parallel ribbons with shorter repeat distances.

ribbons can rotate, and this rotation changes the local environment of the water molecules in the adjacent unit cell. When the next water molecules are released, more inter-ribbon hydrogen bonds form, and the cooperative ribbon rotation and water loss repeat as the dehydration front moves from the edges to the center of the crystal. Ribbon rotation is undoubtedly also facilitated by the highly anisotropic thermal expansion, which is 10X larger along the *c*-axis than the *b*-axis. One expects this type of synchronous ribbon rotation and water loss to be initiated at the crystal surface where molecules have fewer nearest neighbors and mobility constraints compared to molecules in the bulk.

Importantly, the 1-D ribbon rotation model also serves to explain the change in the symmetry within the π -stacks of CM and Cd. The dense (100) CM layers are made from antiparallel ribbons with offset π -stacking between molecules. Cooperative rotation of ribbons breaks the two-dimensional π -network in CM but enables ribbons with parallel alignment to π -stack face—face, thereby creating a dense two-dimensional layer in an orthogonal direction, Cd (100) (see also Figure 1B–D) Notably, the repeat distance between 1-D ribbons in Cd (3.81 Å) is shorter than in CM (3.89 Å), so water loss also enables stronger π - π interactions to be realized. While water loss in the CM-to-Cd transformation forces obvious changes in the

hydrogen bonding motif, the changes in the π - π interactions are equally significant.

While least-motion arguments³¹ have been invoked to explain solid-state reactions for half a century, there was no guarantee that such arguments would necessarily apply here, since the volume change in going from CM to Cd is quite large (18.3%). The proposed ribbon-rotation model does assume a high degree of correlated motion, but it is consistent with the time-resolved sPXRD data, which shows direct conversion, the highly anisotropic thermal expansion, and other kinetic and optical data that points to the importance of reaction initiation on the crystal surface. The ribbon-rotator model is also consistent with previous reports, which indicate water removal through enantiotropic CM faces yields Cd with opposite handedness.

Rehydration—Cd to CM. To demonstrate true "switch-like" behavior, the rehydration reaction was also investigated. Anhydrous cytosine was previously reported to transform to CM at RH \geq 70%, ¹⁴ though here the goal was to assess if this reverse reaction generally follows the same mechanistic path. sPXRD and DVS experiments performed under high-humidity conditions were used to assess the mechanism and kinetics of the Cd-to-CM rehydration reaction.

To assess structural changes with sPXRD, high-humidity air was generated by bubbling the He gas through an aqueous solution before it entered the flow cell. Though the exact RH of the air was not known, it was expected to be > 70%. Using Cd generated from a previous dehydration experiment, sPXRD patterns were collected continuously at 25 °C as the humid He gas was passed through the sample. The Cd-to-CM transformation occurred in a few minutes, and there was no evidence of any intermediate crystalline phases in the rehydration process (Figures S6 and S7).

For kinetic analyses, we turned to DVS experiments where more precise control of the relative humidity was possible. Cd rehydration experiments conducted at 25 °C and 75, 85, and 95 RH % showed progressively faster kinetics as the humidity level was increased, with average rate constants of 0.003, 0.008, and 0.030 min⁻¹, respectively (Figure 8). Replicate measurements of

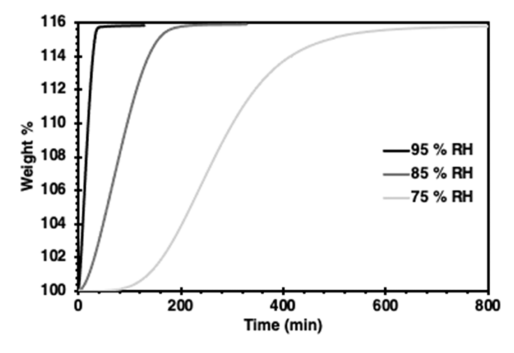


Figure 8. DVS rehydration of Cd at 75, 85, and 95% RH.

rehydration at 75% RH were collected and fit to the kinetic models in Table 1. In all datasets, nucleation and growth models ($R^2 > 0.999$) and geometrical contraction models ($R^2 > 0.99$) fit the data well (Table S4). We note that the experimental data were a poor fit to diffusion models, indicating that rehydration is also a surface-mediated process.

To further demonstrate the switch-like nature of the dehydration—rehydration reaction, Cd was cycled between 95% RH (120 min) and 5% RH (600 min) (Figure 9). DVS data indicated that complete rehydration of Cd to CM at 95% RH

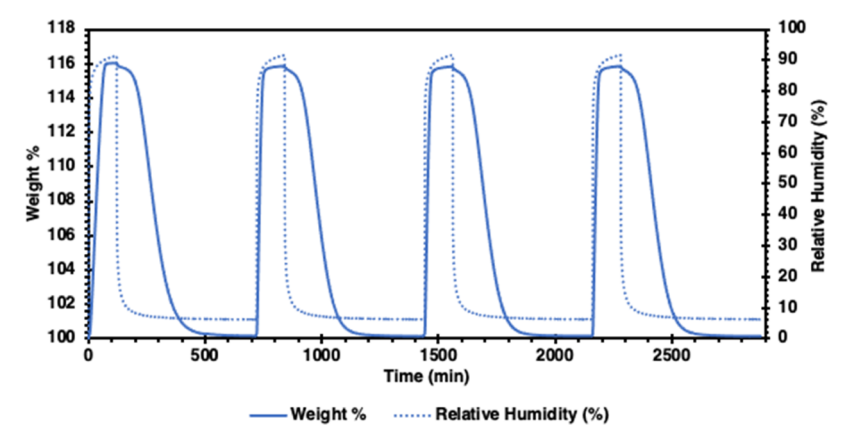


Figure 9. Reversible Cd to CM cycling between at 25 °C under DVS conditions. Rehydration of Cd to CM at 95% RH and dehydration of CM to Cd at 5% RH can be repeated multiple times without any apparent change in the reaction kinetics.

occurred within \sim 40 min at 25 °C, while complete dehydration of CM to Cd at 5% RH required longer time periods. The hydration—dehydration reaction kinetics over multiple cycles proved to be highly reproducible. The Cd-to-CM transformation may occur via the microscopically reversible rotation of 1-D ribbons, though it seems unlikely this is the only mechanistic route back to CM. The conditions where dehydration and rehydration occur are not equivalent, and under high-humidity conditions, it is reasonable to expect that the overall reaction can be affected by other factors, e.g., wettability of the surfaces. Multiple rehydration pathways back to CM may be possible, potentially even through water droplet condensation—recrystallization processes on Cd particle surfaces. 32

CONCLUSIONS

Through this work, we have presented a detailed characterization of the solid-state dehydration of CM to Cd and the subsequent rehydration of Cd to CM. Using time-resolved sPXRD and Rietveld refinement methods, we determined this is a one-step conversion that does not involve intermediate phases. That CM does not show any premature changes in its cell dimensions prior to conversion indicates that water loss occurs synchronously with anhydrate formation. A molecular-level "switch-like" mechanism consistent with all experimental data is proposed wherein water loss and cooperative rotation of onedimensional ribbons enable the solid to toggle between orthogonal π -networks with different symmetry. The suite of complementary characterization techniques employed sPXRD, thermogravimetric analyses, moisture sorption, and microscopy—also serves to highlight how the material processing may impact reaction kinetics, especially for reactions that are initiated on crystal surfaces. These effects are important to consider when attempting to get a holistic understanding of any solid-state reaction.

ASSOCIATED CONTENT

Supporting Information

The Supporting Information is available free of charge at https://pubs.acs.org/doi/10.1021/acs.cgd.2c01014.

SEM, DSC, optical microscopy, and data tables (PDF)

Accession Codes

CCDC 2205653-2205657 contain the supplementary crystallographic data for this paper. These data can be obtained free of

charge via www.ccdc.cam.ac.uk/data_request/cif, or by emailing data_request@ccdc.cam.ac.uk, or by contacting The Cambridge Crystallographic Data Centre, 12 Union Road, Cambridge CB2 1EZ, UK; fax: +44 1223 336033.

AUTHOR INFORMATION

Corresponding Author

Jennifer A. Swift — Department of Chemistry, Georgetown University, Washington, District of Columbia 20057-1227, United States; orcid.org/0000-0002-8011-781X; Email: jas2@georgetown.edu

Authors

Megan E. Fleming — Department of Chemistry, Georgetown University, Washington, District of Columbia 20057-1227, United States

Taylor A. Watts — Department of Chemistry, Georgetown University, Washington, District of Columbia 20057-1227, United States

Kelly A. McKenna — Department of Chemistry, Georgetown University, Washington, District of Columbia 20057-1227, United States

Elizabeth K. Miehls — Department of Chemistry, Georgetown University, Washington, District of Columbia 20057-1227, United States

Complete contact information is available at: https://pubs.acs.org/10.1021/acs.cgd.2c01014

Author Contributions

[†]M.E.F. and T.A.W. shared first-authorship.

Notes

The authors declare no competing financial interest.

ACKNOWLEDGMENTS

The authors are grateful for financial support provided by the National Science Foundation (DMR 1609541 and 2004435). They thank Travis Holman for the use of his research group's ball mill, Jeff Bertke for his help with single-crystal XRD, and Andrey Yakovenko and Marina Solomos for their assistance with collecting synchrotron data. This research used resources of the Advanced Photon Source, a U.S. Department of Energy (DOE) Office of Science User Facility operated for the DOE Office of Science by Argonne National Laboratory under Contract No. DE-AC02-06CH11357.

REFERENCES

- (1) Khawam, A.; Flanagan, D. R. Solid-State Kinetic Models: Basics and Mathematical Fundamentals. *J. Phys. Chem. B* **2006**, *110*, 17315–17328
- (2) Galwey, A. K. Structure and order in thermal dehydrations of crystalline solids. *Thermochim. Acta* **2000**, 355, 181–238.
- (3) Petit, S.; Coquerel, G. Mechanism of Several Solid-Solid Transformations between Dihydrated and Anhydrous Copper(II) 8-Hydroxyquinolinates. Proposition for a Unified Model for the Dehydration of Molecular Crystals. *Chem. Mater.* 1996, 8, 2247–2258.
- (4) Bacchi, A.; Bosetti, E.; Carcelli, M.; Pelagatti, P.; Rogolino, D.; Pelizzi, G. "Venetian Blinds" Mechanism of Solvation/Desolvation in Palladium(II) Wheel-and-Axle Organic—Inorganic Diols. *Inorg. Chem.* **2005**, *44*, 431–442.
- (5) Bērziņš, A.; Actiņš, A. Dehydration of mildronate dihydrate: a study of structural transformations and kinetics. *CrystEngComm* **2014**, 16, 3926–3934.
- (6) Hédoux, A.; Paccou, L.; Derollez, P.; Guinet, Y. Dehydration mechanism of caffeine hydrate and structural description of driven metastable anhydrates analyzed by micro Raman spectroscopy. *Int. J. Pharm.* **2015**, *486*, 331–338.
- (7) Jeffrey, G. A.; Kinoshita, Y. The crystal structure of cytosine monohydrate. *Acta Crystallogr.* **1963**, *16*, 20–28.
- (8) Barker, D. L.; Marsh, R. E. The crystal structure of cytosine. *Acta Crystallogr.* **1964**, *17*, 1581–1587.
- (9) Perrier, P.; Byrn, S. R. Influence of crystal packing on the solidstate desolvation of purine and pyrimidine hydrates: loss of water of crystallization from thymine monohydrate, cytosine monohydrate, 5nitrouracil monohydrate, and 2'-deoxyadenosine monohydrate. *J. Org. Chem.* **1982**, *47*, 4671–4676.
- (10) Martel, P.; Powell, B. M. Dehydration of cytosine monohydrate at physiological temperatures. *Biophys. J.* **1983**, *41*, 91–93.
- (11) Kawasaki, T.; Hakoda, Y.; Mineki, H.; Suzuki, K.; Soai, K. Generation of Absolute Controlled Crystal Chirality by the Removal of Crystal Water from Achiral Crystal of Nucleobase Cytosine. *J. Am. Chem. Soc.* **2010**, *132*, 2874–2875.
- (12) Mineki, H.; Kaimori, Y.; Kawasaki, T.; Matsumoto, A.; Soai, K. Enantiodivergent formation of a chiral cytosine crystal by removal of crystal water from an achiral monohydrate crystal under reduced pressure. *Tetrahedron: Asymmetry* **2013**, *24*, 1365–1367.
- (13) Braun, D. E.; Griesser, U. J. Prediction and experimental validation of solid solutions and isopolymorphs of cytosine/5-flucytosine. *CrystEngComm* **2017**, *19*, 3566–3572.
- (14) Braun, D. E.; Kahlenberg, V.; Griesser, U. J. Experimental and Computational Hydrate Screening: Cytosine, 5-Flucytosine, and Their Solid Solution. *Cryst. Growth Des.* **2017**, *17*, 4347–4364.
- (15) Hübschle, C. B.; Sheldrick, G. M.; Dittrich, B. ShelXle: a Qt graphical user interface for SHELXL. *J. Appl. Crystallogr.* **2011**, 44, 1281–1284.
- (16) Chupas, P. J.; Chapman, K. W.; Kurtz, C.; Hanson, J. C.; Lee, P. L.; Grey, C. P. A versatile sample-environment cell for nonambient X-ray scattering experiments. *J. Appl. Crystallogr.* **2008**, *41*, 822–824.
- (17) Toby, B. H.; Von Dreele, R. B. GSAS-II: the genesis of a modern open-source all purpose crystallography software package. *J. Appl. Crystallogr.* **2013**, *46*, 544–549.
- (18) Coelho, A. A. TOPAS and TOPAS-Academic: an optimization program integrating computer algebra and crystallographic objects written in C++. *J. Appl. Crystallogr.* **2018**, *51*, 210–218.
- (19) Mittemeijer, E. J.; Welzel, U. Modern Diffraction Methods; Wiley-VCH, 2012.
- (20) Müller, M.; Dinnebier, R. E.; Jansen, M.; Wiedemann, S.; Plüg, C. Kinetic analysis of the phase transformation from α to β -copper phthalocyanine: A case study for sequential and parametric Rietveld refinements. *Powder Diffr.* **2009**, 24, 191–199.
- (21) Müller, M.; Dinnebier, R. E.; Jansen, M.; Wiedemann, S.; Plüg, C. The influence of temperature, additives and polymorphic form on the kinetics of the phase transformations of copper phthalocyanine. *Dyes Pigm.* **2010**, *85*, 152–161.

- (22) Friedman, H. L. Kinetics of thermal degradation of char-forming plastics from thermogravimetry. Application to a phenolic plastic. *J. Polym. Sci., Part C: Polym. Symp.* **2007**, *6*, 183–195.
- (23) Ismail, A. F., Khulbe, K. C.; Matsura, T. Gas Separation Membranes: Polymeric and Inorganic; Springer International, 2015.
- (24) Agbada, C. O.; York, P. Dehydration of theophylline monohydrate powder effects of particle size and sample weight. *Int. J. Pharm.* 1994, 106, 33–40.
- (25) Taylor, L. S.; York, P. Effect of particle size and temperature on the dehydration kinetics of trehalose dihydrate. *Int. J. Pharm.* **1998**, *167*, 215–221.
- (26) Peterson, K. E.; Henry, R. F.; Zhang, G. G. Z.; MacGillivray, L. R. Reducing a cocrystal to nanoscale dimensions enables retention of physical crystal integrity upon dehydration. *CrystEngComm* **2017**, *19*, 3723–3726.
- (27) Watts, T. A.; Miehls, E. K.; Swift, J. A. Time-Resolved Cooperative Motions in the Solid-State Dehydration of Thymine Hydrate. *Cryst. Growth Des.* **2020**, *20*, 7941–7950.
- (28) Khawam, A.; Flanagan, D. R. Role of isoconversional methods in varying activation energies of solid-state kinetics: I. isothermal kinetic studies. *Thermochim. Acta* **2005**, 429, 93–102.
- (29) Koradia, V.; de Diego, H. L.; Elema, M. R.; Rantanen, J. Integrated Approach to Study the Dehydration Kinetics of Nitrofurantoin Monohydrate. *J. Pharm. Sci.* **2010**, *99*, 3966–3976.
- (30) Zhou, D.; Schmitt, E. A.; Zhang, G. G.; Law, D.; Wight, C. A.; Vyazovkin, S.; Grant, D. J. Model-free treatment of the dehydration kinetics of nedocromil sodium trihydrate. *J. Pharm. Sci.* **2003**, *92*, 1367–1376.
- (31) Schmidt, G. M. J. Photodimerization in the Solid State. *Pure Appl. Chem.* **1971**, *27*, 647–678.
- (32) Zellelow, A. Z.; Kim, K.-H.; Sours, R. E.; Swift, J. A. Solid State Dehydration of Uric Acid Dihydrate. *Cryst. Growth Des.* **2010**, *10*, 418–425.

☐ Recommended by ACS

Phase Transition of Hypoxanthinium Nitrate Monohydrate

Małgorzata Katarzyna Cabaj and Paulina Maria Dominiak

NOVEMBER 21, 2020

CRYSTAL GROWTH & DESIGN

READ 🗹

Visualization of Nonequilibrium Properties of a Crystalline Polymer: Formation of Ring-Lite Due to the Gibbs-Thomson Effect and Dark-Ring Due to the Melting Point Inversion

Koji Nishida, Masahiro Ohshima, et al.

NOVEMBER 16, 2021

CRYSTAL GROWTH & DESIGN

READ 🗹

Experimental Evidence of Slow Mode Water in the Vicinity of Poly(ethylene oxide) at Physiological Temperature

Taiki Tominaga, Hideki Seto, et al.

FEBRUARY 22, 2022

THE JOURNAL OF PHYSICAL CHEMISTRY B

READ 🗹

Parts-per-Million Detection of Trace Crystal Forms Using AF-PTIR Microscopy

Aleksandr Razumtcev, Garth J. Simpson, et al.

SEPTEMBER 13, 2022

ANALYTICAL CHEMISTRY

READ 🗹

Get More Suggestions >